Research Square

Preprints are preliminary reports that have not undergone peer review.
They should not be considered conclusive, used to inform clinical practice,
or referenced by the media as validated information.

Dynamic analysis of multilayered glass slab under pedestrian excitation

Hamza Aliyu
Huai'an University
Yanan Gao
gaoyn@hau.edu.cn
Huai'an University
Ntasha Chimpampwe
Huai'an University
Peng Zhang
Huai'an University
Shijun Chen
Jiangsu Meicheng Architectural & Planning Design Institute Co., Ltd.

Research Article

Keywords: Laminated glass walkway, PVB interlayer degradation, Pedestrian-induced vibration, Closed-form solution, Finite element analysis, Vibration serviceability

Posted Date: November 3rd, 2026

DOI: https://doi.org/10.21203/rs.3.rs-11373218/v1

License: This work is licensed under a Creative Commons Attribution 4.0 International License.
Read Full License

Additional Declarations: No competing interests reported.

Dynamic analysis of multilayered glass slab under pedestrian excitation

Abstract

Laminated glass walkways depend on their polyvinyl butyral (PVB) interlayers to make the glass plies act together, yet PVB loses stiffness with temperature, load duration and age. This study examines how interlayer degradation changes the dynamic behaviour of a five-layer laminated glass panel under pedestrian excitation. A multilayer thin-plate formulation gives the neutral-surface position and the layer-wise bending and torsional rigidities, and the equation of motion under a sequence of moving bipedal footfalls is solved in closed form by modal superposition and the Laplace transform. Frequency bounds for full and zero composite action, together with a partial-interaction estimate, relate the interlayer shear modulus to the natural frequencies. A three-dimensional finite element model of a panel based on an in-service glass footbridge is then analysed by modal, harmonic response and full transient analyses, for a rigid-bond and a degraded interlayer with the same geometry, supports, mesh, damping and loading. The closed-form time histories agree closely with the transient finite element results, and the partial-interaction estimate reproduces the finite element frequencies of the bending modes. Degradation lowers every natural frequency, the higher modes most, and amplifies the displacement, velocity and acceleration produced by walking. Velocity and acceleration grow more than displacement because the lowered fundamental frequency moves towards a walking harmonic. The principal stress in the glass also rises but stays far below the strength of fully tempered glass, and the deflection remains within the adopted limit; the peak acceleration of the degraded panel, however, exceeds the recommended comfort limit. Vibration serviceability, rather than glass strength or deflection, therefore governs the degraded panel. Because the frequency bounds need only geometry and elastic properties, a measured fundamental frequency can be used to screen the condition of the interlayer without destructive testing.

Keywords: Laminated glass walkway; PVB interlayer degradation; Pedestrian-induced vibration; Closed-form solution; Finite element analysis; Vibration serviceability

Nomenclature

Symbol	Description	Unit
A_{in}, B_{in}	Coefficients of the steady-state response of mode i to load harmonic n	s²
$\mathbf{B}$	Strain–displacement matrix	m^{-1}
b	Width of the beam model, $b = L_y$	m
$\mathbf{C}$	Global damping matrix	N·s/m
c	Viscous damping coefficient per unit area	N·s/m³
D	Bending rigidity of the layered section	N·m
D_{xy}	Poisson coupling rigidity of the layered section	N·m
D_κ	Torsional rigidity of the layered section	N·m
$\mathbf{D}_e$	Elasticity matrix of the layer material	Pa
DLF_n	Dynamic load factor of the n-th load harmonic	–
d	Distance between the centroids of adjacent glass plies, $d = h_g + t_{\mathrm{int}}$	m
E, E_α	Elastic modulus; elastic modulus of layer α	Pa
E_g	Elastic modulus of glass	Pa
E_{PVB}	Elastic modulus of the PVB interlayer	Pa
EI	Flexural rigidity of the beam model	N·m²
EI_{comp}	Flexural rigidity for full composite action (monolithic section)	N·m²
$EI_{\mathrm{eff},i}$	Effective flexural rigidity of the i-th bending mode with partial interaction	N·m²
EI_{ind}	Flexural rigidity of the glass plies bending independently	N·m²
EI_∞	Flexural rigidity of the glass plies with full shear transfer	N·m²
e	Element index	–
$\mathbf{F}(t), \mathbf{F}(\Omega)$	Global load vector; its complex amplitude	N
F_0	Amplitude of the harmonic force	N
$F_k(t)$	Vertical force of the k-th footfall	N
F_τ, F_ι	Footfall forces of the trailing and leading legs, applied at (x_τ, y_τ) and (x_ι, y_ι) (Fig. 1)	N
f, f_i	Natural frequency; natural frequency of mode i (of the i-th vertical bending mode in Eqs. (19)–(23))	Hz
$f_{1,\mathrm{m}}$	Measured fundamental frequency	Hz
$f_{\max}$	Highest frequency resolved in the transient analysis	Hz
f_s	Step frequency	Hz
G	Shear modulus	Pa
$G_{\mathrm{int}}, G_{\mathrm{PVB}}$	Shear modulus of the interlayer; shear modulus of PVB	Pa
$G_{in}(\tau)$	Response of mode i to a unit sine load of frequency ω_n	s²
g	Gravitational acceleration	m/s²
g_i	Shear-coupling parameter of the i-th bending mode	–
$H(\tau)$	Heaviside step function	–
h	Total thickness of the laminate	m

Symbol	Description	Unit
h_0	Depth of the neutral surface below the top surface	m
h_α	Thickness of layer α	m
h_g, h_j	Thickness of one glass ply; thickness of the j-th glass ply	m
i	Imaginary unit	–
i	Mode number	–
j	Glass ply index (Eqs. (20) and (22)); mode index (Section 2.4 and Eq. (25))	–
$\mathbf{K}$	Global stiffness matrix	N/m
k	Footfall index; time-sample index in Eq. (30)	–
L	Span of the beam model, $L = L_x$	m
L_x	Length of the panel between the supported short edges	m
L_y	Width of the panel between the free long edges	m
$\mathcal{L}\{\cdot\}$	Laplace transform	–
$\mathbf{M}$	Global mass matrix	kg
M^*	Modal mass of the fundamental mode, referred to footprint S3	kg
M_x, M_y	Bending moments per unit width	N·m/m
M_{xy}, M_{yx}	Twisting moments per unit width	N·m/m
m	Total mass of the panel	kg
$\bar{m}$	Mass per unit area	kg/m²
m_L	Mass per unit length, $m_L = m/L_x$	kg/m
m_p	Mass of the pedestrian	kg
$\mathbf{N}$	Matrix of element shape functions	–
N	Number of time samples	–
N_f	Number of footfalls	–
n	Number of layers (Eqs. (2)–(7)); order of the load harmonic (Eqs. (12)–(18))	–
$Q_i(\lambda)$, $R_i(\lambda)$	Laplace transforms of $q_i(t)$ and $r_i(t)$	m·s; m/s
$q_i(t)$	Modal coordinate of mode i	m
R^2	Coefficient of determination	–
$r_i(t)$	Modal force of mode i per unit modal mass	m/s²
T_e	Contact duration of one footfall, $T_e = T_s/0.76$	s
T_s	Step period, $T_s = 1/f_s$	s
t	Time	s
t_k	Start time of the k-th footfall	s
t_{int}	Thickness of one interlayer	m
$\mathbf{U}(\Omega)$	Complex displacement amplitude vector	m
$\lvert U\rvert$, $\lvert V\rvert$, $\lvert A\rvert$	Displacement, velocity and acceleration amplitudes of the harmonic response	m; m/s; m/s²
$\mathbf{u}$, $\dot{\mathbf{u}}$, $\ddot{\mathbf{u}}$	Nodal displacement, velocity and acceleration vectors	m; m/s; m/s²

Symbol	Description	Unit
u_z, v_z, a_z	Vertical displacement, velocity and acceleration in the global system of the FE model (Z upwards)	m; m/s; m/s²
V_e	Volume of element e	m³
$w(x, y, t)$	Deflection of the plate, positive downwards	m
$X, X_{\mathrm{FE}}, X_{\mathrm{ref}}$	Peak value of a response quantity; peak value from the FE and reference (closed-form) solutions	varies
x, y, z	Coordinates along the span, across the width and through the thickness (z measured downwards from the neutral surface)	m
x_k, y_k	Coordinates of the k-th footprint	m
$x_{\mathrm{FE},k}, x_{\mathrm{ref},k}$	k-th time sample of the FE and reference histories	varies
$\bar{x}_{\mathrm{ref}}$	Mean of the reference history	varies
Z	Vertical axis of the global coordinate system of the FE model, positive upwards	–
z_α	Coordinate of the lower surface of layer α	m
Greek symbols		
α	Layer index ($\alpha = 1, \ldots, n$); Rayleigh mass-proportional damping coefficient, Eq. (28)	–; s^{-1}
β	Rayleigh stiffness-proportional damping coefficient, Eq. (28)	s
β_{N}	Parameter of the Newmark method (β_{N} = 1/4)	–
γ	Layer index in Eqs. (2) and (3); parameter of the Newmark method (γ = 1/2)	–
Δ_{in}	Denominator in Eq. (18)	s^{-4}
Δf	Frequency increment of the harmonic response analysis	Hz
Δt	Time step of the transient analysis	s
δ	Relative difference between peak values, Eq. (30)	%
$\delta(\cdot)$	Dirac delta function	m^{-1}
δ_{ij}	Kronecker delta	–
κ	Curvature of the neutral surface	m^{-1}
λ	Laplace variable	s^{-1}
ν, ν_α	Poisson's ratio; Poisson's ratio of layer α	–
ξ, ξ_i	Damping ratio; damping ratio of mode i	–
ρ, ρ_α	Density; density of layer α	kg/m³
σ_x, σ_y	Normal stresses in the x and y directions	Pa
$\sigma_{\alpha x}$	Bending stress in layer α	Pa
σ_1	Maximum principal stress	Pa
τ	Time measured from the application of a load term	s
$\phi_i(x)$	Mode shape function of mode i in the analytical model	–
$\boldsymbol{\phi}_i$	Mass-normalised mode shape vector of mode i in the FE model	kg$^{-1/2}$
Ω	Circular excitation frequency	rad/s
ω_i	Circular natural frequency of mode i	rad/s

Symbol	Description	Unit
ω_{di}	Damped circular natural frequency of mode i	rad/s
ω_n	Circular frequency of the n-th load harmonic, $\omega_n = 0.76\, n\pi f_s$	rad/s
Subscripts and superscripts		
comp	Full composite action	
d	Damped	
e	Element	
eff	Effective (partial interaction)	
FE	Finite element solution	
g	Glass	
ind	Independent plies	
int	Interlayer	
m	Measured	
max	Maximum	
N	Newmark	
ref	Reference (closed-form) solution	
T	Transpose	
∞	Full shear transfer	
$\dot{(\,)}$, $\ddot{(\,)}$	First and second derivatives with respect to time	
Abbreviations		
APDL	ANSYS Parametric Design Language	
DG	Degraded interlayer scenario	
DLF	Dynamic load factor	
FE	Finite element	
FRF	Frequency response function	
FT	Fully tempered (glass)	
MAE	Mean absolute error	
MSUP	Mode superposition	
PVB	Polyvinyl butyral	
RB	Rigid-bond interlayer scenario	
S1–S5	Footprint patches along the centreline (S3 at mid-span)	

1. Introduction

Structural glass is now common in floors, stairs, roofs, viewing platforms and pedestrian walkways, where it carries load while keeping the structure visually open (Feldmann et al., 2014). Glass is brittle, so laminated glass walkways have to be designed for their behaviour both before and after fracture (ASTM International, 2021; CEN, 2021). Glass panels are also light and slender, and their serviceability is often governed by vibration rather than by stress: users may feel unsafe on a panel long before the glass comes close to its strength (Bedon and Fasan, 2019; Bedon and Mattei, 2021). For pedestrian structures, vibration checks therefore matter as much as strength checks, particularly when a natural frequency approaches the

walking frequency or one of its harmonics (Bachmann and Ammann, 1987; Živanović et al., 2005). Field studies on glass walkways and glass suspension footbridges confirm that restraint conditions, damping, user perception and vibration mitigation dominate their practical assessment (Bedon and Fasan, 2019; Bedon et al., 2019; Gong et al., 2021).

In laminated glass, the plies are bonded by a polymer interlayer that transfers shear between them, holds the fragments together after breakage and largely controls the bending stiffness of the section. Polyvinyl butyral (PVB), the most widely used interlayer, is viscoelastic: its shear modulus falls with temperature, load duration and ageing, and rises with loading frequency (López-Aenlle and Pelayo, 2014). The same panel can therefore behave almost monolithically under short loads at low temperature and come close to a stack of independent plies once the interlayer softens. Design guidance, effective-thickness methods and layer-wise finite element (FE) models have been developed to deal with this behaviour (CNR, 2013; Feldmann et al., 2014; Galuppi and Royer-Carfagni, 2012), and dynamic effective-thickness formulations show how interlayer viscoelasticity shifts the natural frequencies and damping of laminated beams and plates (López-Aenlle and Pelayo, 2014; Pelayo and López-Aenlle, 2019). Post-breakage tests on in-service pedestrian laminated glass units further suggest that the resulting frequency shift can be used to detect damage and to estimate the residual stiffness (Bedon and Noè, 2021).

Standards and guidance documents cover glass products, characteristic strength, load resistance and vibration serviceability to different degrees (ASTM International, 2016; CEN, 2002, 2005, 2015, 2021; CNR, 2013; ISO, 2007; Sétra, 2006). Real glass floors and walkways, however, contain details that do not fit simple formulas, such as flexible support strips, un-bonded sacrificial layers, partial contact and steel bracing. For existing structures, field testing and numerical updating are therefore valuable, as shown for the glass suspension footbridge in the Basilica of Aquileia and for other in-service pedestrian glass systems (Bedon, 2019; Bedon and Bergamo, 2019; Bedon and Fasan, 2019; Bedon and Noè, 2021).

Human walking can be modelled at several levels of detail. Deterministic Fourier-series models describe the vertical ground reaction force through the dynamic load factors (DLFs) of the walking harmonics and form the basis of most design guidance (Bachmann and Ammann, 1987; Racic et al., 2009; Ramoul and Spremić, 2021; Van Nimmen et al., 2014). More advanced models include gait variability, crowd effects and human–structure interaction (Caprani et al., 2012; Qin et al., 2013; Shahabpoor et al., 2016). When the fundamental frequency of a floor exceeds about four times the step frequency, its response to each footfall

is essentially transient, and the contact duration and the timing of successive footfalls become important (Smith et al., 2009; Willford and Young, 2006). This study uses a deterministic footfall model in which each footfall is a truncated Fourier series acting over a finite contact duration (Fan et al., 2012), applied at the actual footprint positions of a pedestrian crossing the panel.

Despite this body of work, little attention has been paid to how interlayer degradation affects the response of laminated glass walkways to walking, expressed as displacement, velocity and acceleration rather than as a change in natural frequency alone. Analytical solutions that carry the layered section through the forced-vibration problem are also scarce. This paper addresses both gaps for a five-layer laminated glass panel based on an in-service glass footbridge and makes three contributions. (i) A multilayer thin-plate formulation with layer-wise rigidities is presented, and its equation of motion under a sequence of moving bipedal footfalls is solved in closed form by modal superposition and the Laplace transform, giving displacement, velocity and acceleration histories. (ii) A three-dimensional layer-wise FE model is analysed by modal, harmonic response and full transient analyses for a rigid-bond and a degraded interlayer under otherwise identical conditions; the governing equation of each FE step is stated, and the transient results are checked against the closed-form solution. (iii) Frequency bounds for full and zero composite action and a partial-interaction estimate are shown to reproduce the FE frequencies of the bending modes. Because they need only geometry and elastic properties, a measured frequency can be inverted to estimate the interlayer shear modulus, which provides a simple non-destructive screening tool.

The rest of the paper is organised as follows. Section 2 develops the analytical formulation, and Section 3 describes the FE model and the analysis procedures. Section 4 presents the modal, harmonic and transient results together with their verification. Section 5 discusses how interlayer degradation affects the natural frequencies, the kinematic response, the glass stress and serviceability, and Section 6 summarises the conclusions.

2. Analytical formulation

Fig. 1 shows the multilayer glass plate of length L_x, width L_y and total thickness h loaded by a walking pedestrian. The plate has n layers ($n = 5$, Fig. 2), numbered $\alpha = 1, \dots, n$ from the top surface, each with thickness h_α, elastic modulus E_α, Poisson's ratio ν_α and density ρ_α. The coordinate z is measured downwards from the neutral surface, and the deflection $w(x, y, t)$ is positive downwards, in the direction of the footfall loads. Three assumptions are

made: (i) deflections are small and the materials are linear elastic; (ii) the laminate as a whole follows Kirchhoff thin-plate kinematics; and (iii) adjacent layers are perfectly bonded, so that plane sections remain plane through the whole thickness (Kim, 2004). Assumption (iii) is relaxed in Section 2.7, where partial shear interaction through a soft interlayer is considered.

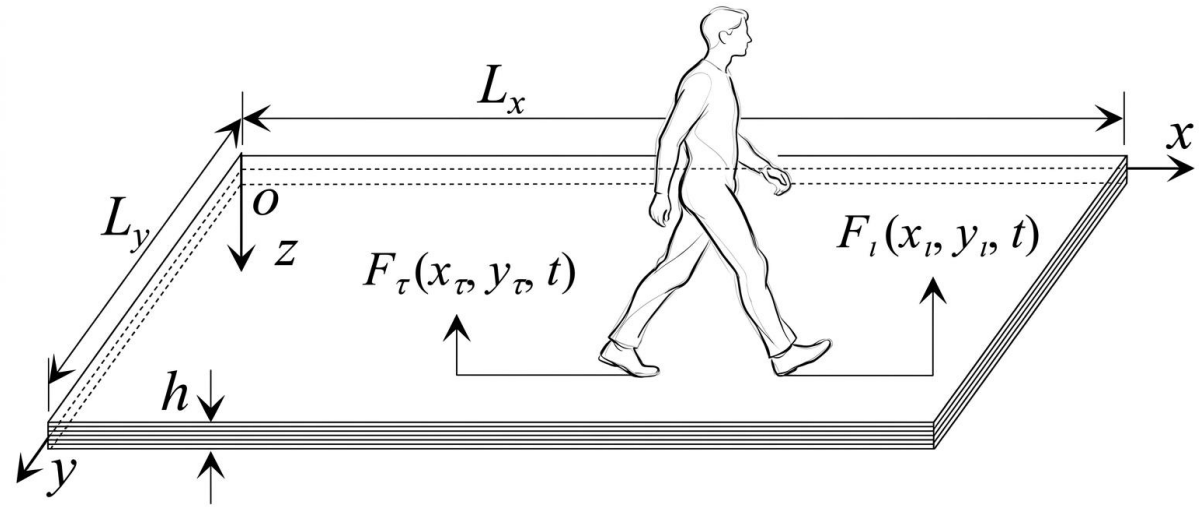


Fig. 1. Multilayer laminated glass plate under the footfall loads of a walking pedestrian (F_τ: trailing leg; F_l: leading leg; thickness exaggerated).

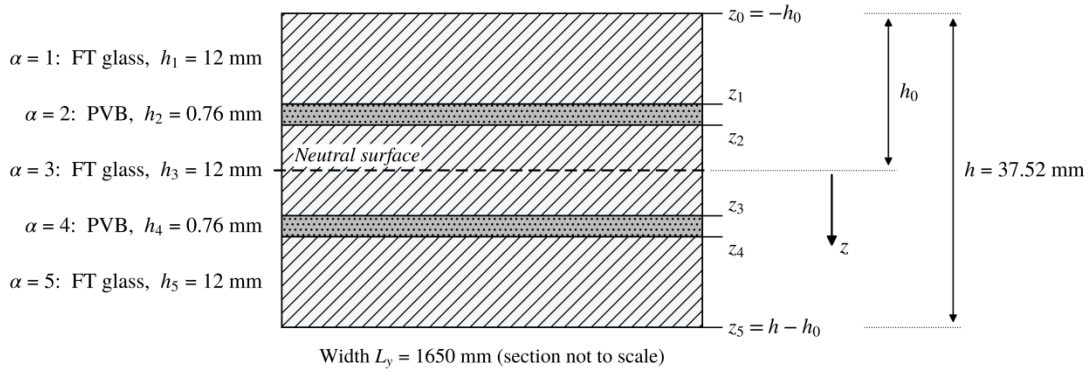


Fig. 2. Cross-section of the five-layer laminated glass panel and the notation used in Section 2 (layer thicknesses not to scale).

2.1 Neutral surface position

Under assumption (iii), the bending stress in layer α is proportional to its distance from the neutral surface:

$$\sigma_{\alpha x} = E_\alpha \, \kappa \, z \tag{1}$$

where κ is the curvature of the neutral surface. The neutral surface is located by the condition that the resultant axial force over the section vanishes:

$$\sum_{\alpha=1}^{n} E_\alpha \int_{z_{\alpha-1}}^{z_\alpha} z \, \mathrm{d}z = 0, \qquad z_\alpha = \sum_{\gamma=1}^{\alpha} h_\gamma - h_0 \tag{2}$$

where h_0 is the depth of the neutral surface below the top surface, so that $z_0 = -h_0$ and $z_n = h - h_0$ (Fig. 2). Evaluating the integrals gives (Zhang et al., 2015)

$$h_0 = \frac{\sum_{\alpha=1}^{n} E_\alpha \, h_\alpha^2 + 2\sum_{\alpha=2}^{n}\sum_{\gamma=1}^{\alpha-1} E_\alpha \, h_\alpha h_\gamma}{2\sum_{\alpha=1}^{n} E_\alpha \, h_\alpha} \tag{3}$$

For the symmetric lay-up considered here, Eq. (3) gives $h_0 = h/2$ for any ratio of the glass and interlayer moduli.

2.2 Internal forces and layer-wise rigidities

For a plate element of sides $\mathrm{d}x$ and $\mathrm{d}y$, the bending moments M_x and M_y and the twisting moment M_{xy} per unit width are

$$M_x = \int_{-h_0}^{h-h_0} \sigma_x \, z \, \mathrm{d}z = -D\frac{\partial^2 w}{\partial x^2} - D_{xy}\frac{\partial^2 w}{\partial y^2} \tag{4a}$$

$$M_y = \int_{-h_0}^{h-h_0} \sigma_y \, z \, \mathrm{d}z = -D\frac{\partial^2 w}{\partial y^2} - D_{xy}\frac{\partial^2 w}{\partial x^2} \tag{4b}$$

$$M_{xy} = M_{yx} = -2D_\kappa \frac{\partial^2 w}{\partial x \, \partial y} \tag{4c}$$

The bending rigidity D, the Poisson coupling rigidity D_{xy} and the torsional rigidity D_κ of the layered section are obtained by integrating the layer moduli multiplied by z^2 through the thickness, with z measured from the neutral surface at depth h_0 (Eq. (3)):

$$D = \frac{1}{3}\sum_{\alpha=1}^{n} \frac{E_\alpha}{1-\nu_\alpha^2}(z_\alpha^3 - z_{\alpha-1}^3) \tag{5a}$$

$$D_{xy} = \frac{1}{3}\sum_{\alpha=1}^{n} \frac{E_\alpha \, \nu_\alpha}{1-\nu_\alpha^2}(z_\alpha^3 - z_{\alpha-1}^3) \tag{5b}$$

$$D_\kappa = \frac{1}{3}\sum_{\alpha=1}^{n} \frac{E_\alpha}{2(1+\nu_\alpha)}(z_\alpha^3 - z_{\alpha-1}^3) \tag{5c}$$

For a homogeneous plate, Eqs. (5) reduce to the familiar relations $D_{xy} = \nu D$ and $D_\kappa = (1-\nu)D/2$.

2.3 Equation of motion

Vertical equilibrium of the plate element gives

$$\bar{m}\frac{\partial^2 w}{\partial t^2} + c\frac{\partial w}{\partial t} = \frac{\partial^2 M_x}{\partial x^2} + 2\frac{\partial^2 M_{xy}}{\partial x\,\partial y} + \frac{\partial^2 M_y}{\partial y^2} + \sum_{k=1}^{N_f} F_k(t)\,\delta(x - x_k)\,\delta(y - y_k) \tag{6}$$

where c is the viscous damping coefficient per unit area, $F_k(t)$ is the vertical force of the k-th footfall applied at (x_k, y_k), N_f is the number of footfalls, $\delta(\cdot)$ is the Dirac delta function, which concentrates each footfall at its footprint so that $\iint \delta(x - x_k)\,\delta(y - y_k)\,\mathrm{d}x\,\mathrm{d}y = 1$, and $\bar{m}$ is the mass per unit area:

$$\bar{m} = \sum_{\alpha=1}^{n} \rho_\alpha\, h_\alpha \tag{7}$$

Consecutive footfalls belong alternately to the trailing and leading legs (F_τ and F_l in Fig. 1) and overlap in time during the double-support phase. Substituting Eqs. (4) into Eq. (6) gives

$$\bar{m}\frac{\partial^2 w}{\partial t^2} + c\frac{\partial w}{\partial t} + D\left(\frac{\partial^4 w}{\partial x^4} + \frac{\partial^4 w}{\partial y^4}\right) + 2\left(D_{xy} + 2D_\kappa\right)\frac{\partial^4 w}{\partial x^2\,\partial y^2} = \sum_{k=1}^{N_f} F_k(t)\,\delta(x - x_k)\,\delta(y - y_k) \tag{8}$$

2.4 Modal decomposition

The panel is simply supported along its short edges, $x = 0$ and $x = L_x$, and free along its long edges. For footfalls on the longitudinal centreline, the response is dominated by vertical bending modes that are almost uniform across the width (Section 4.1), while the torsional modes are not excited. The deflection is therefore expanded in beam-type modes that satisfy $w = M_x = 0$ at the supported edges (Yan, 1989):

$$w(x, y, t) = \sum_{i=1}^{\infty} q_i(t)\,\phi_i(x), \qquad \phi_i(x) = \sin\frac{i\pi x}{L_x} \tag{9}$$

Substituting Eq. (9) into Eq. (8), multiplying by ϕ_j, integrating over the plate and using the orthogonality of the modes gives the uncoupled modal equations

$$\ddot{q}_i + 2\xi_i\omega_i\,\dot{q}_i + \omega_i^2\,q_i = r_i(t) \tag{10}$$

with

$$\omega_i^2 = \left(\frac{i\pi}{L_x}\right)^4 \frac{D}{\bar{m}}, \qquad c = 2\bar{m}\,\xi_i\,\omega_i,$$
$$r_i(t) = \frac{2}{m}\sum_{k=1}^{N_f} F_k\,(t)\,\phi_i(x_k), \qquad m = \bar{m}L_xL_y \tag{11}$$

where ξ_i is the modal damping ratio and m is the total mass of the panel; the factor $2/m$ comes from the modal mass, $\iint \bar{m}\,\phi_i^2\,\mathrm{d}x\,\mathrm{d}y = m/2$. Eq. (11) gives the cylindrical-bending frequency. Replacing DL_y by the beam rigidity EI (Section 2.7) allows anticlastic curvature at the free edges, and the two estimates bracket the FE frequency (Section 4.1).

2.5 Footfall load model

The vertical force of each footfall follows the model of Fan et al. (2012): a five-term Fourier series of the pedestrian's weight $m_p g$, with dynamic load factors DLF_n that vary linearly with the step frequency f_s (Table 1). The step period is $T_s = 1/f_s$, and each foot stays in contact for $T_e = T_s/0.76$, so consecutive footfalls overlap during the double-support phase. The k-th footfall starts at $t_k = (k-1)T_s$ and is

$$F_k(t) = \begin{cases} m_p\,g\sum_{n=1}^{5} \mathrm{DLF}_n \sin[\omega_n(t-t_k)], & t_k \le t \le t_k + T_e \\ 0, & \text{otherwise} \end{cases} \tag{12}$$

$$\omega_n = 0.76\,n\,\pi f_s \tag{13}$$

so that $\omega_n T_e = n\pi$ and every term vanishes at the beginning and at the end of the contact. Using the time-shifting property, the Laplace transform of Eq. (12) is

$$\mathcal{L}\{F_k(t)\} = m_p\,g\sum_{n=1}^{5} \mathrm{DLF}_n\,\frac{\omega_n}{\lambda^2+\omega_n^2}\left[e^{-t_k\lambda} - (-1)^n e^{-(t_k+T_e)\lambda}\right] \tag{14}$$

where λ is the Laplace variable.

Table 1. Dynamic load factors of the footfall model (Fan et al., 2012).

DLF	$1.6 \le f_s \le 2.32$ **Hz**	$2.32 < f_s \le 2.4$ **Hz**	**Value at** $f_s =$ 2.0 **Hz**
DLF_1	$-0.0698f_s + 1.211$	$-0.1784f_s + 1.463$	1.0714
DLF_2	$0.1052f_s - 0.1284$	$-0.4716f_s + 1.210$	0.0820
DLF_3	$0.3002f_s - 0.1534$	$-0.0118f_s + 0.5703$	0.4470
DLF_4	$0.0416f_s - 0.0288$	$-0.2600f_s + 0.6711$	0.0544
DLF_5	$-0.0275f_s + 0.0608$	$-0.0906f_s + 0.2132$	0.0058

2.6 Closed-form solution

With $Q_i(\lambda) = \mathcal{L}\{q_i(t)\}$ and $R_i(\lambda) = \mathcal{L}\{r_i(t)\}$, the Laplace transform of Eq. (10) is

$$Q_i(\lambda) = \frac{R_i(\lambda) + (\lambda + 2\xi_i\omega_i)q_i(0) + \dot{q}_i(0)}{\lambda^2 + 2\xi_i\omega_i\lambda + \omega_i^2} \tag{15}$$

For a panel initially at rest ($q_i(0) = \dot{q}_i(0) = 0$), substituting Eqs. (11) and (14) into Eq. (15) and performing the inverse transform gives the closed-form modal response

$$q_i(t) = \frac{2m_p\, g}{m} \sum_{k=1}^{N_f} \phi_i\,(x_k) \sum_{n=1}^{5} \mathrm{DLF}_n\,[G_{in}(t - t_k) - (-1)^n\, G_{in}(t - t_k - T_e)] \tag{16}$$

in which $G_{in}(\tau)$ is the response of mode i to a unit sine load of frequency ω_n applied at $\tau = 0$:

$$\begin{aligned} G_{in}(\tau) \quad &= H(\tau)(A_{in}\sin\omega_n\tau + B_{in}\cos\omega_n\tau) \\ &\quad + H(\tau)\, e^{-\xi_i\omega_i\tau}\left[-B_{in}\cos\omega_{di}\tau - \frac{\xi_i\omega_i B_{in} + \omega_n A_{in}}{\omega_{di}}\sin\omega_{di}\tau\right] \end{aligned} \tag{17}$$

$$\begin{aligned} A_{in} &= \frac{\omega_i^2 - \omega_n^2}{\Delta_{in}}, \qquad B_{in} = \frac{-2\xi_i\omega_i\omega_n}{\Delta_{in}}, \\ \Delta_{in} &= (\omega_i^2 - \omega_n^2)^2 + (2\xi_i\omega_i\omega_n)^2, \qquad \omega_{di} = \omega_i\sqrt{1 - \xi_i^2} \end{aligned} \tag{18}$$

where $H(\tau)$ is the Heaviside step function. The first two terms of Eq. (17) are the steady-state response to the n-th harmonic, and the exponential term is the free vibration needed to satisfy the zero initial conditions; the second G_{in} term in Eq. (16) removes the load at the end of the contact. The deflection then follows from Eq. (9), and the velocity and acceleration from the analytical time derivatives of Eq. (17). All results are given in the global coordinate system of the FE model (Z upwards), so a downward displacement is negative, $u_z = -w$.

Eq. (16) was implemented in MATLAB and checked against a fourth-order Runge–Kutta integration of Eq. (10) under the same load. Over the whole time history, the largest difference in mid-span displacement was 3.9×10^{-6} mm for the rigid-bond panel and 1.1×10^{-5} mm for the degraded panel.

2.7 Frequency bounds and partial interaction

Treating the panel as a simply supported beam of span $L = L_x$ and mass per unit length $m_L = m/L_x$, the frequency of the i-th vertical bending mode is

$$f_i = \frac{i^2\pi}{2L^2}\sqrt{\frac{EI}{m_L}} \tag{19}$$

Two limiting rigidities follow from the perfect-bond and no-bond assumptions:

$$EI_{\text{comp}} = \frac{E_g\, b\, h^3}{12}, \qquad EI_{\text{ind}} = E_g\, b \sum_{j=1}^{3} \frac{h_j^3}{12} \tag{20}$$

where $b = L_y$, E_g is the modulus of glass and h_j are the glass ply thicknesses. EI_{comp} corresponds to a monolithic section of thickness h (full composite action, i.e. the rigid-bond scenario, in which the interlayers have the modulus of glass), and EI_{ind} to three plies bending independently (no shear transfer). The perfect-bond rigidities of Eqs. (5) cannot represent a soft interlayer, because they enforce plane sections across it whatever its modulus. For an interlayer of finite shear modulus G_{int} and thickness t_{int}, the partial-interaction theory of layered beams (Newmark et al., 1951), applied to a symmetric three-ply laminate with sinusoidal mode shapes, gives the effective rigidity of the i-th bending mode as

$$EI_{\text{eff},i} = EI_{\text{ind}} + (EI_{\infty} - EI_{\text{ind}})\frac{g_i}{1+g_i} \tag{21}$$

$$EI_{\infty} = E_g\, b\left[\sum_{j=1}^{3}\frac{h_j^3}{12} + 2h_g d^2\right], \qquad g_i = \frac{G_{\text{int}}}{t_{\text{int}}\, E_g\, h_g (i\pi/L)^2} \tag{22}$$

where EI_{∞} is the rigidity of the glass plies with full shear transfer, h_g is the thickness of one glass ply, $d = h_g + t_{\text{int}}$ is the distance between the centroids of adjacent plies and g_i is a shear-coupling parameter. Because g_i decreases with i^2, the composite action, and hence the frequency, of the higher bending modes is reduced more strongly than that of the fundamental mode. Conversely, a measured fundamental frequency $f_{1,\text{m}}$ gives $EI_{\text{eff},1}$ through Eq. (19), and Eq. (21) can be inverted to estimate the apparent shear modulus of the interlayer:

$$\begin{aligned} G_{\text{int}} &= \frac{t_{\text{int}}\, E_g\, h_g\, \pi^2}{L^2}\,\frac{EI_{\text{eff},1} - EI_{\text{ind}}}{EI_{\infty} - EI_{\text{eff},1}}, \\ EI_{\text{eff},1} &= m_L\left(\frac{2L^2 f_{1,\text{m}}}{\pi}\right)^2 \end{aligned} \tag{23}$$

3. Finite element model

3.1 Reference panel and interlayer scenarios

The panel studied here is based on the suspended glass footbridge inside the Basilica of Aquileia, Italy (Bedon and Bergamo, 2019). Its central-nave panels are L_x = 2.65 m long between the two supported short edges and L_y = 1.65 m wide between the two free long edges (Fig. 3a). The load-bearing laminate is made of three 12 mm fully tempered (FT) glass plies and two 0.76 mm PVB interlayers, with a total thickness of 37.52 mm (Fig. 2). The un-bonded 6 mm annealed sacrificial layer on top of the real panels, the steel tendons and the support details are not modelled. The model is therefore used to compare interlayer conditions with each other, not to reproduce the measured frequency of the central-nave panel (14.97 Hz), which also reflects support and system effects outside the scope of the simplified model (Bedon and Bergamo, 2019).

Two interlayer scenarios are compared (Table 2). The glass plies have the same elastic modulus, E = 70 GPa, in both. In the rigid-bond (RB) scenario, the PVB is given the elastic properties of glass, so the laminate behaves as a monolithic section and represents the upper bound of composite action. In the degraded (DG) scenario, the PVB has E = 4 MPa and ν = 0.49, i.e. G_{PVB} = 1.34 MPa, which represents a long-term or degraded interlayer. Geometry, supports, mesh, damping and loading are the same in both scenarios, so any difference in response comes from the interlayer alone.

Table 2. Layer properties of the two interlayer scenarios.

Layer (α)	Material	Thickness (mm)	E	ν	G	ρ (kg/m³)
1, 3, 5	FT glass (both scenarios)	12.00	70 GPa	0.23	28.46 GPa	2500
2, 4	PVB, rigid bond (RB)	0.76	70 GPa	0.23	28.46 GPa	1100
2, 4	PVB, degraded (DG)	0.76	4 MPa	0.49	1.34 MPa	1100

3.2 Geometry, mesh and boundary conditions

The panel was modelled in ANSYS Workbench 2024 R1 (ANSYS Inc., 2024) following the workflow in Fig. 4. The five layers were created as solid bodies with shared topology, which gives a conformal mesh with perfect bond at the four glass–PVB interfaces and avoids contact elements. Five 200 mm × 100 mm footprint patches were imprinted on the top face along the centreline (y = 0.825 m) at x_k = 0.125 + 0.6(k − 1) m, k = 1, …, 5 (Fig. 3a), which places footprint S3 at mid-span. The mesh (Fig. 5) uses 20-node quadratic hexahedral elements

(SOLID186) generated by the MultiZone method with a 40 mm element size. There are two elements through the thickness of each glass ply and one through each interlayer, giving 101,341 nodes and 22,512 elements. The model mass, 400.84 kg, matches the hand-calculated value. Both end faces (all five layers) are restrained vertically (u_z = 0), and the bottom edge at x = 0 is also restrained in the x and y directions to prevent rigid-body motion. The short edges are therefore simply supported and the long edges are free.

Mesh convergence was checked by repeating the RB modal analysis with element sizes from 50 mm down to 20 mm (Table 3). Between the 40 mm and 20 mm meshes, the first three natural frequencies changed by less than 0.002%, while the solution time grew about ninefold. The 40 mm mesh was therefore used for all analyses.

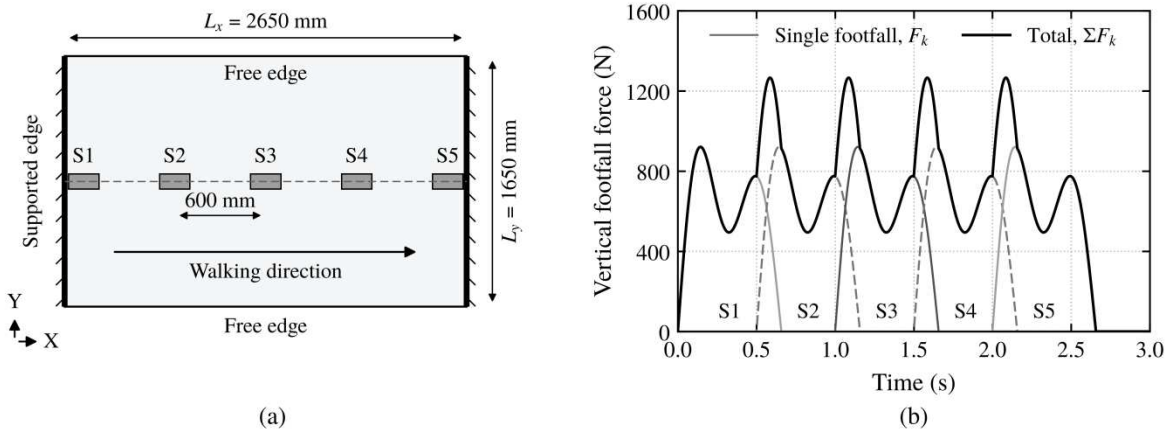


Fig. 3. Footfall load model: (a) plan of the panel with supports and footprints S1–S5; (b) vertical force histories of the five footfalls (Eq. (12); m_p = 80 kg, f_s = 2.0 Hz) and their sum.

Table 3. Mesh convergence of the RB modal analysis.

Element size (mm)	Nodes	Elements	f_1 (Hz)	f_2 (Hz)	f_3 (Hz)	Solution time (s)
50	63,468	13,992	13.0665	31.4277	52.5168	27
40 (adopted)	101,341	22,512	13.0665	31.4273	52.5168	44
30	175,086	39,160	13.0664	31.4269	52.5167	262[a]
20	391,998	88,312	13.0664	31.4268	52.5164	399

3.3 Loading

For the transient analysis, the five footfall forces of Eq. (12) were applied with m_p = 80 kg, f_s = 2.0 Hz (T_s = 0.5 s, T_e = 0.658 s) and a step length of 0.6 m, which corresponds to normal walking for an adult (Pachi and Ji, 2005). Each force was applied as a uniform pressure history on its footprint patch through APDL command objects, so that the resultant on

footprint k equals $F_k(t)$ (Fig. 3b). Each footfall peaks at 920.9 N and carries an impulse of 401.5 N·s, and the crossing takes 2.658 s. For the harmonic response analysis, a sinusoidal force with a reference amplitude of F_0 = 235.4 N ($0.3m_pg$) was applied downwards on footprint S3 and swept over 1–25 Hz. The system is linear, so the harmonic responses scale with F_0 and the comparison between the two scenarios does not depend on its value.

3.4 Analysis procedures

Fig. 4 shows the FE workflow with the governing equation of each analysis step, and Table 4 compares the three FE processes. After meshing, the element stiffness and mass matrices are assembled into the global matrices (Bathe, 1996; Cook et al., 2002)

$$\mathbf{K} = \sum_e \int_{V_e} \mathbf{B}^{\mathrm{T}}\, \mathbf{D}_e\, \mathbf{B}\, \mathrm{d}V, \qquad \mathbf{M} = \sum_e \int_{V_e} \rho\, \mathbf{N}^{\mathrm{T}}\mathbf{N}\, \mathrm{d}V \tag{24}$$

where $\mathbf{N}$ is the matrix of shape functions, $\mathbf{B}$ the strain–displacement matrix and $\mathbf{D}_e$ the elasticity matrix of the layer material.

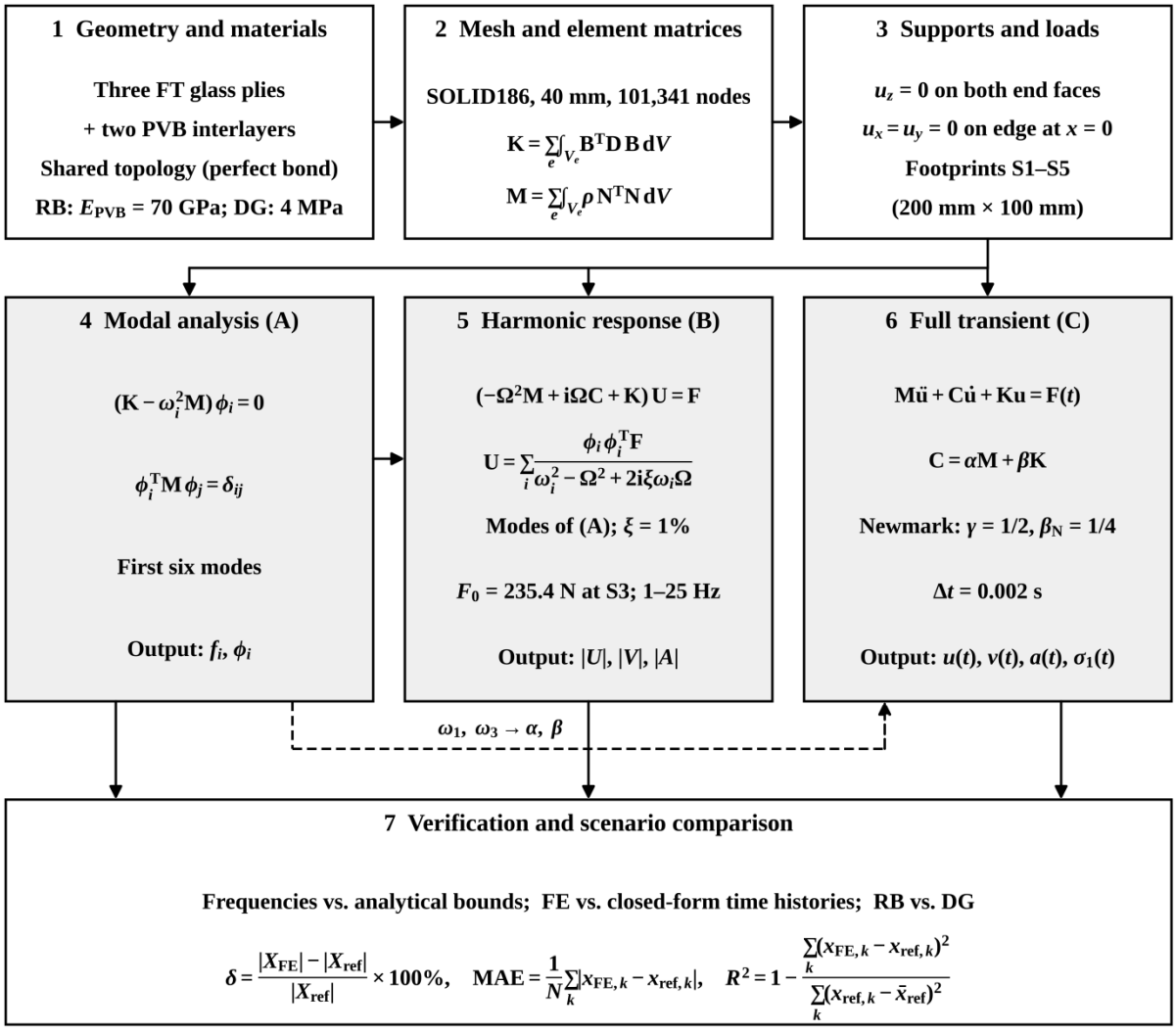


Fig. 4. Finite element workflow with the governing equation of each analysis step.

Modal analysis. The undamped natural frequencies and mass-normalised mode shapes of the first six modes follow from the eigenvalue problem

$$(\mathbf{K} - \omega_i^2 \mathbf{M})\boldsymbol{\phi}_i = \mathbf{0}, \qquad \boldsymbol{\phi}_i^T \mathbf{M}\, \boldsymbol{\phi}_j = \delta_{ij} \tag{25}$$

Harmonic response analysis. The mode-superposition (MSUP) harmonic analysis uses the modes of Eq. (25) to solve

$$\begin{aligned} &(-\Omega^2 \mathbf{M} + \mathrm{i}\,\Omega\, \mathbf{C} + \mathbf{K})\mathbf{U}(\Omega) = \mathbf{F}(\Omega), \\ &\mathbf{U}(\Omega) = \sum_{i=1}^{6} \frac{\boldsymbol{\phi}_i\, \boldsymbol{\phi}_i^T \mathbf{F}}{\omega_i^2 - \Omega^2 + 2\mathrm{i}\,\xi\,\omega_i\,\Omega} \end{aligned} \tag{26}$$

where Ω is the excitation frequency, $\mathbf{U}$ the complex displacement amplitude and ξ = 1% the constant damping ratio of all modes (Chopra, 2017; Clough and Penzien, 1993). The range 1–25 Hz was divided into 960 intervals (Δf = 0.025 Hz), and the first natural frequency was

added as a user-defined frequency so that the resonance peak is captured exactly. The velocity and acceleration amplitudes are then $|V| = \Omega|U|$ and $|A| = \Omega^2|U|$.

Transient analysis. The full transient analysis integrates the equation of motion

$$\mathbf{M\ddot{u}} + \mathbf{C\dot{u}} + \mathbf{Ku} = \mathbf{F}(t), \qquad \mathbf{C} = \alpha\mathbf{M} + \beta\mathbf{K} \tag{27}$$

with Rayleigh damping calibrated to ξ = 1% at modes 1 and 3, the first two vertical bending modes:

$$\alpha = \frac{2\xi\,\omega_1\,\omega_3}{\omega_1 + \omega_3}, \qquad \beta = \frac{2\xi}{\omega_1 + \omega_3} \tag{28}$$

This gives α = 1.3148 s^{-1} and β = 4.8535 × 10^{-5} s for the RB panel and α = 0.9676 s^{-1} and β = 7.8207 × 10^{-5} s for the DG panel. The damping ratios of the other modes then lie between 0.8% and 1.9% (Table 5). Eq. (27) was integrated by the Newmark average-acceleration method (γ = 1/2, β_{N} = 1/4) with the sparse direct solver; the method is unconditionally stable and introduces no numerical damping (Bathe, 1996; Newmark, 1959). The time step satisfies

$$\Delta t \le \frac{1}{20 f_{\max}} \tag{29}$$

so Δt = 0.002 s resolves frequencies up to $f_{\max}$ = 25 Hz with at least 20 steps per cycle. The analysis covers 3.5 s: the crossing (2.658 s) followed by free vibration.

Outputs and comparison metrics. The vertical displacement, velocity and acceleration were taken as averages over footprint S3 (mid-span), and the maximum principal stress as the largest value in the three glass plies. The FE results were compared with the closed-form solution of Section 2.6 through the relative peak difference δ, the coefficient of determination R^2 and the mean absolute error MAE:

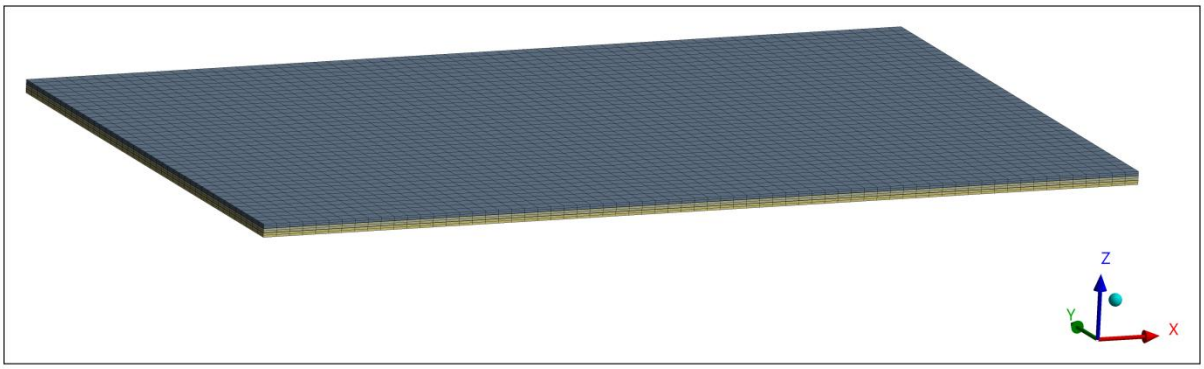
$$\delta = \frac{|X_{\mathrm{FE}}| - |X_{\mathrm{ref}}|}{|X_{\mathrm{ref}}|} \times 100\%, \qquad \mathrm{MAE} = \frac{1}{N}\sum_{k=1}^{N}\left|x_{\mathrm{FE},k} - x_{\mathrm{ref},k}\right|,$$
$$R^2 = 1 - \frac{\sum_{k=1}^{N}\left(x_{\mathrm{FE},k} - x_{\mathrm{ref},k}\right)^2}{\sum_{k=1}^{N}\left(x_{\mathrm{ref},k} - \bar{x}_{\mathrm{ref}}\right)^2} \tag{30}$$

where X denotes a peak value, x_k the k-th of N time samples and $\bar{x}_{\mathrm{ref}}$ the mean of the reference history.

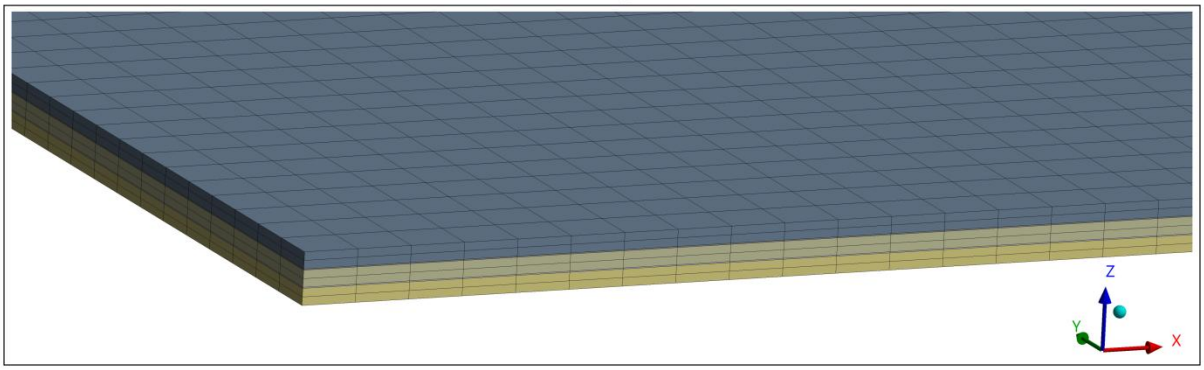
Table 4. Comparison of the three FE analysis processes.

Item	Modal (A)	Harmonic response (B)	Full transient (C)
Governing equation	Eq. (25)	Eq. (26)	Eqs. (27)–(28)

Item	Modal (A)	Harmonic response (B)	Full transient (C)
Solution method	Eigenvalue extraction (program-controlled solver)	Mode superposition of the six modes of (A)	Direct integration, Newmark γ = 1/2, β_N = 1/4; sparse direct solver
Damping	None	Constant ratio ξ = 1%	Rayleigh, ξ = 1% at modes 1 and 3
Load	None	F_0 = 235.4 N at S3	$F_k(t)$, k = 1–5, on footprints S1–S5
Resolution	Six modes	1–25 Hz, Δf = 0.025 Hz	0–3.5 s, Δt = 0.002 s
Main outputs	f_i, $\boldsymbol{\phi}_i$	$\lvert U\rvert$, $\lvert V\rvert$, $\lvert A\rvert$ and σ_1 amplitude versus frequency	$u_z(t)$, $v_z(t)$, $a_z(t)$, $\sigma_1(t)$, support reactions
Role in this study	Dynamic properties; basis for (B) and Rayleigh constants of (C)	Resonant sensitivity of the two scenarios	Response to walking; verification against Eq. (16)



(a) Whole panel



(b) Corner detail: two elements through each glass ply and one through each interlayer

Fig. 5. Finite element mesh (SOLID186, 40 mm element size): (a) whole panel; (b) corner detail showing two elements through the thickness of each glass ply and one through each interlayer.

4. Results

4.1 Modal analysis

Table 5 lists the first six natural frequencies of the two panels, and Fig. 6 shows the mode shapes of the DG panel. The mode sequence is the same for both panels: first vertical bending, first torsion, second vertical bending, second torsion, first transverse bending and third vertical bending. The first mode carries 81% of the total mass in the vertical direction

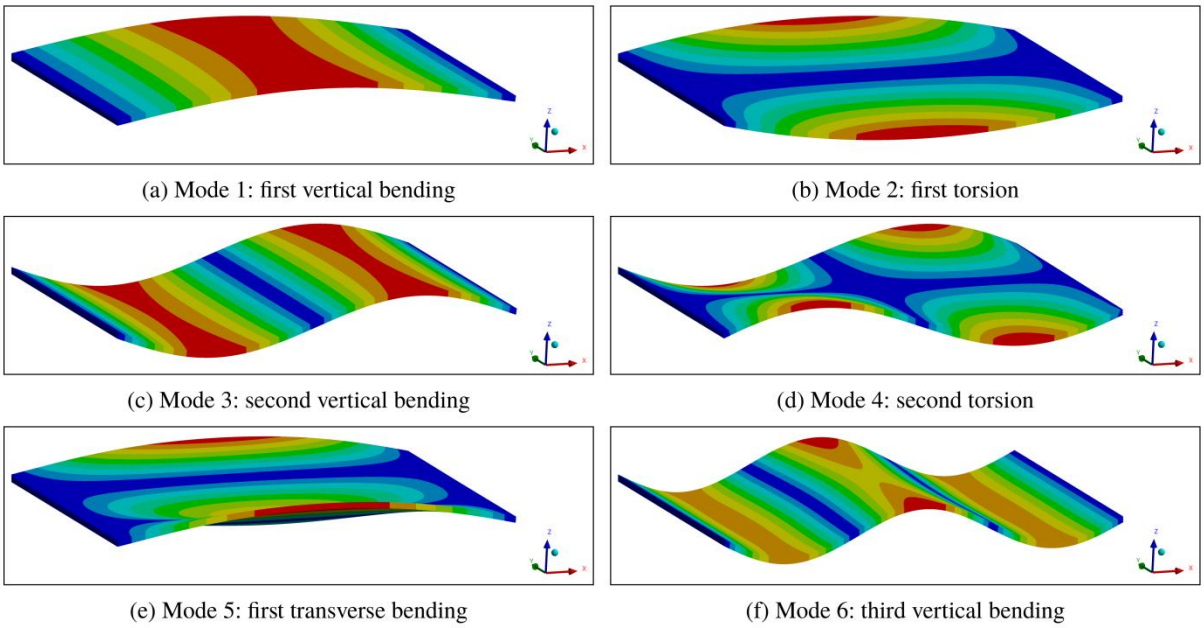
(RB panel) and is nearly uniform across the width, which justifies the beam-type modes of Eq. (9).

Interlayer degradation lowers the fundamental frequency from 13.066 Hz to 10.313 Hz (−21.1%) and the frequencies of modes 2–6 by 42–53%. The reduction grows with the modal wavenumber: a shorter half-wavelength produces larger shear strains in the interlayer and hence a greater loss of composite action, which is the i^{-2} dependence of g_i in Eq. (22). In the DG panel, the third bending mode (55.78 Hz) also comes close to the first transverse bending mode (54.98 Hz).

Table 5. Natural frequencies and Rayleigh damping ratios of the two panels.

Mode	Mode shape	f, RB (Hz)	f, DG (Hz)	f_{DG}/f_{RB}	ξ, RB (%)[a]	ξ, DG (%)[a]
1	First vertical bending	13.066	10.313	0.789	1.00	1.00
2	First torsion	31.427	17.988	0.572	0.81	0.87
3	Second vertical bending	52.517	30.388	0.579	1.00	1.00
4	Second torsion	75.317	39.299	0.522	1.29	1.16
5	First transverse bending	100.55	54.977	0.547	1.64	1.49
6	Third vertical bending	118.04	55.781	0.473	1.89	1.51

[a] Rayleigh damping of the transient analysis, Eq. (28); the harmonic analysis uses ξ = 1% for all modes.



(a) Mode 1: first vertical bending

(b) Mode 2: first torsion

(c) Mode 3: second vertical bending

(d) Mode 4: second torsion

(e) Mode 5: first transverse bending

(f) Mode 6: third vertical bending

Fig. 6. First six mode shapes of the degraded-PVB panel; the rigid-bond panel has the same mode sequence (frequencies in Table 5).

Table 6 compares the FE frequencies of the three vertical bending modes with Eqs. (19)–(22). For the RB panel, the full-composite estimate is 0.8–1.2% below the FE frequencies, while

the cylindrical-bending estimate of Eq. (11) gives 13.32 Hz for the fundamental mode (+2.0%), so the two simplified estimates bracket the FE value. For the DG panel, the perfect-bond rigidity EI_∞ would give 12.88 Hz, 25% above the FE value; a perfect-bond formulation clearly cannot represent a soft interlayer. The partial-interaction estimate of Eq. (21) reproduces the DG frequencies within 0.9% and the DG/RB frequency ratios of all three bending modes within 0.8%. Applying Eq. (23) to the FE fundamental frequency of the DG panel returns an apparent interlayer shear modulus of 1.36 MPa, within 1.1% of the value assigned in the model (1.34 MPa).

Table 6. Analytical and FE frequencies of the vertical bending modes.

Quantity	$i = 1$	$i = 2$	$i = 3$
FE mode number	1	3	6
RB: FE (Hz)	13.066	52.517	118.04
RB: Eq. (19) with EI_{comp} (Hz)	12.97	51.87	116.71
RB: difference (%)[a]	−0.75	−1.23	−1.13
DG: FE (Hz)	10.313	30.388	55.781
DG: Eq. (21), shear parameter g_i	1.496	0.374	0.166
DG: Eq. (19) with $EI_{\mathrm{eff},i}$ (Hz)	10.29	30.24	55.32
DG: difference (%)[a]	−0.18	−0.50	−0.82
No interaction: Eq. (19) with EI_{ind} (Hz)	4.06	16.25	36.56
Ratio DG/RB: FE / analytical	0.789 / 0.794	0.579 / 0.583	0.473 / 0.474

[a](analytical − FE)/FE × 100%. EI_{comp} = 508,381 N·m², EI_∞ = 501,226 N·m², EI_{ind} = 49,896 N·m², m_L = 151.26 kg/m, G_{int} = 1.342 MPa.

4.2 Harmonic response

Fig. 7 shows the frequency response functions (FRFs) of the vertical displacement, velocity and acceleration at the mid-span footprint S3, and Table 7 lists the resonance peaks. Each FRF has one dominant peak, at the fundamental frequency. A force on the centreline does not excite the torsional modes, the second bending mode has a node at mid-span, and the remaining modes lie above the 25 Hz limit of the sweep. The damping ratio identified from the half-power bandwidth of the peaks is 1.00% for both panels, equal to the input value, which confirms that the sweep resolves the resonance.

Degradation increases the resonant displacement amplitude by 61% (8.28 mm to 13.37 mm) and the velocity amplitude by 27% (0.680 m/s to 0.866 m/s), while the acceleration amplitude is practically unchanged (55.8 m/s² and 56.1 m/s²). Single-mode resonance explains this pattern. The resonant acceleration, $F_0/(2\xi M^*)$, depends only on the modal mass M^* and the damping ratio, neither of which is changed by degradation ($M^* \approx 210$ kg, about $0.52m$, for

both panels). The velocity and displacement, in contrast, scale with $1/\omega_1$ and $1/\omega_1^2$, and the ratios of these quantities between the two panels, 1.27 and 1.61, match the FE results. The maximum principal stress amplitude in the glass rises from 16.35 MPa to 18.59 MPa (+14%). Fig. 8 shows the displacement and stress contours at resonance; the largest deflection, −8.88 mm for RB and −14.22 mm for DG, occurs at mid-span. These harmonic amplitudes correspond to a force held at resonance indefinitely. They describe the sensitivity of the two panels and are not used in the serviceability checks, which are based on the transient response to walking (Sections 4.3, 4.4 and 5.4).

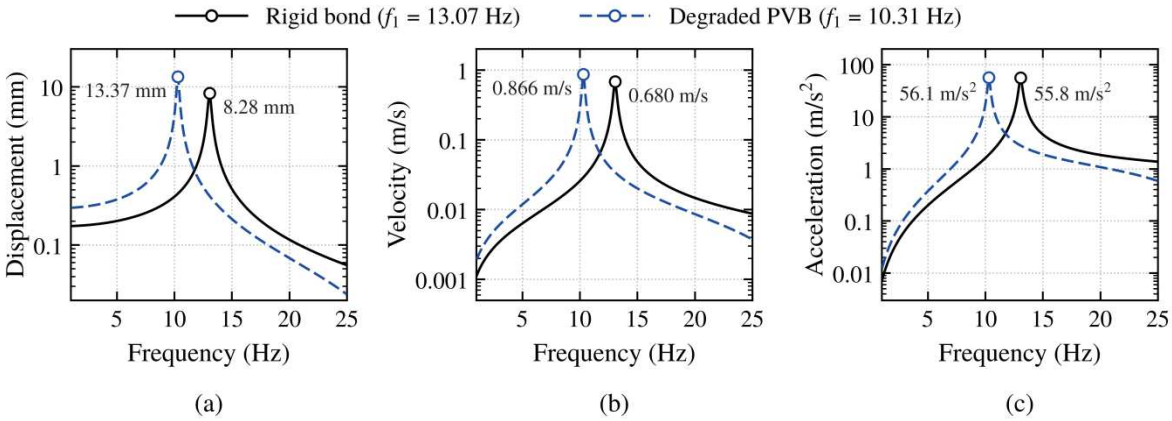
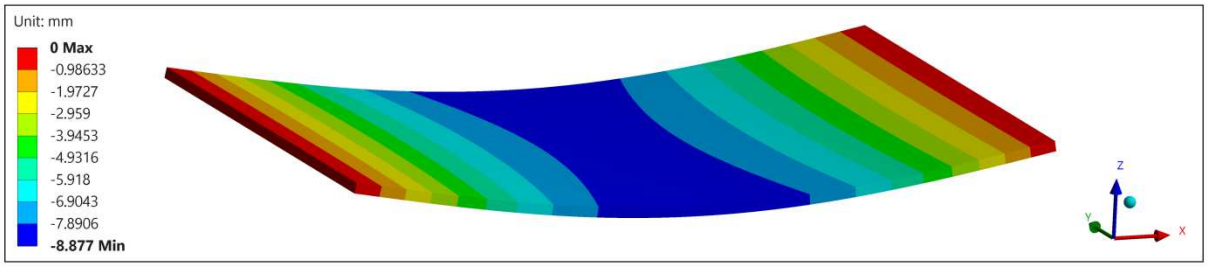


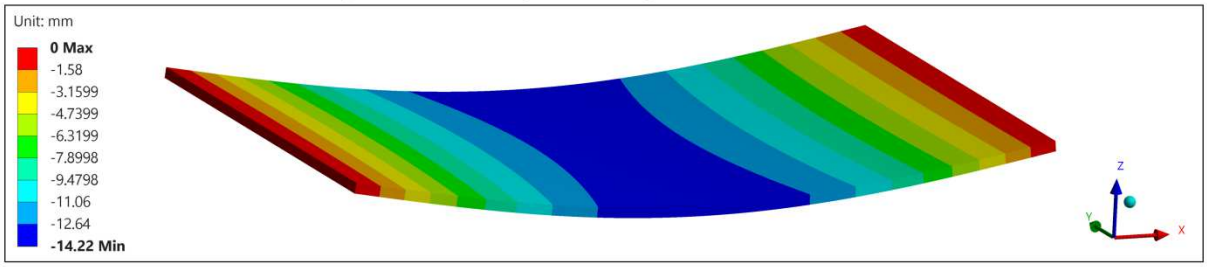
Fig. 7. Frequency response functions at the mid-span footprint S3 for F_0 = 235.4 N: (a) displacement; (b) velocity; (c) acceleration.

Table 7. Resonance peaks of the harmonic response (F_0 = 235.4 N at S3).

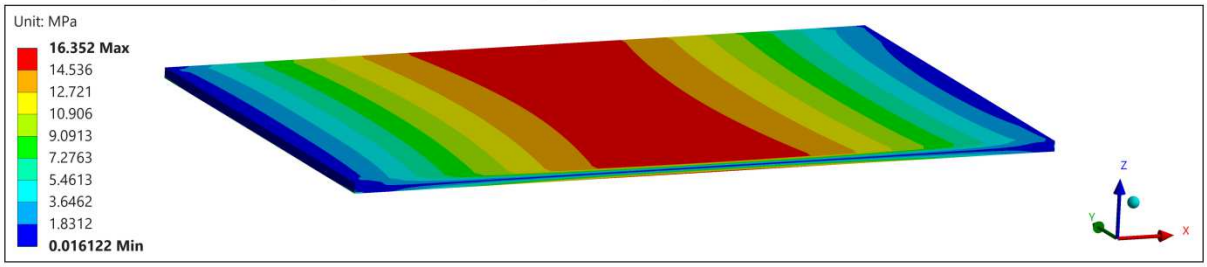
Quantity	**RB**	**DG**	**DG/RB**
Resonance frequency (Hz)	13.067	10.313	0.789
Displacement amplitude at S3 (mm)	8.28	13.37	1.61
Velocity amplitude at S3 (m/s)	0.680	0.866	1.27
Acceleration amplitude at S3 (m/s²)	55.8	56.1	1.01
Half-power damping ratio (%)	1.00	1.00	–
Largest vertical displacement of the panel (mm)	−8.88	−14.22	1.60
Maximum principal stress in the glass (MPa)	16.35	18.59	1.14



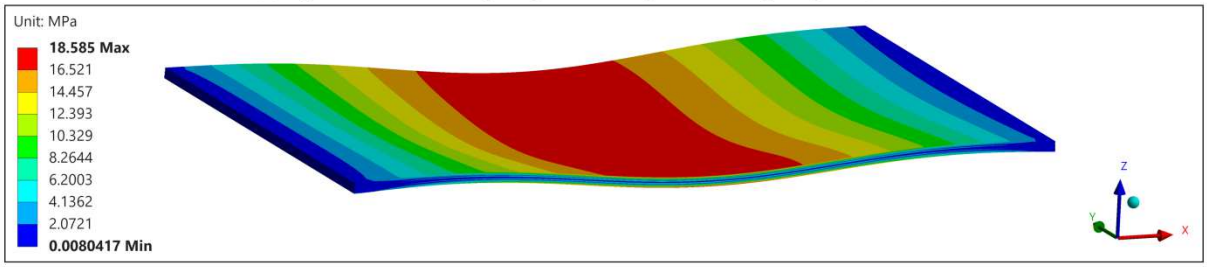
(a) Rigid bond: vertical displacement amplitude at resonance (13.07 Hz)



(b) Degraded PVB: vertical displacement amplitude at resonance (10.31 Hz)



(c) Rigid bond: maximum principal stress amplitude in the glass plies (13.07 Hz)



(d) Degraded PVB: maximum principal stress amplitude in the glass plies (10.31 Hz)

Fig. 8. Harmonic response at resonance (F_0 = 235.4 N at S3): vertical displacement amplitude (a, b) and maximum principal stress amplitude in the glass plies (c, d) of the rigid-bond and degraded-PVB panels. Deformed shapes are exaggerated for visibility.

4.3 Transient response: verification

The load application in the transient analysis was first checked through the impulse balance. For both panels, the time integral of the total vertical support reaction over 0–3.5 s equals the applied impulse of 2007.6 N·s within 0.04%. Figs. 9 and 10 compare the FE time histories at S3 with the closed-form solution of Eq. (16), evaluated with the fundamental mode only (ω_1 from Table 5, ξ_1 = 1%), and Table 8 lists the comparison metrics.

For the RB panel, the peak displacement, velocity and acceleration of the two solutions differ by 1.6%, 3.1% and 2.0%, with $R^2 \geq 0.976$ for all three quantities. For the DG panel, the displacement and velocity differ by 3.9% and 3.1% (R^2 = 0.992), but the FE peak acceleration

exceeds the single-mode value by 16% (R^2 = 0.968). Two simplifications in the closed-form solution account for these differences. First, the sine mode of Eq. (9) slightly overestimates the participation of the footfalls near the supports. A least-squares decomposition of the FE displacement into the responses to the individual footfalls gives participation factors of 0.139 for S1 and S5 and 0.731 for S2 and S4 in the RB panel, compared with 0.148 and 0.758 from the sine mode. Second, the single-mode solution leaves out the higher modes. These modes are much lower in the DG panel (Table 5), so the rapid onset of each footfall excites them more strongly; in the DG panel the participation factor of the mid-span footfall rises to 1.096, against 1.001 in the RB panel. Since the higher modes contribute more to acceleration than to displacement, the single-mode solution captures the displacement and velocity of both panels but underestimates the peak acceleration of the DG panel. The comparison thus confirms the FE transient model and its loading, and shows that the closed-form solution gives reliable estimates of displacement and velocity.

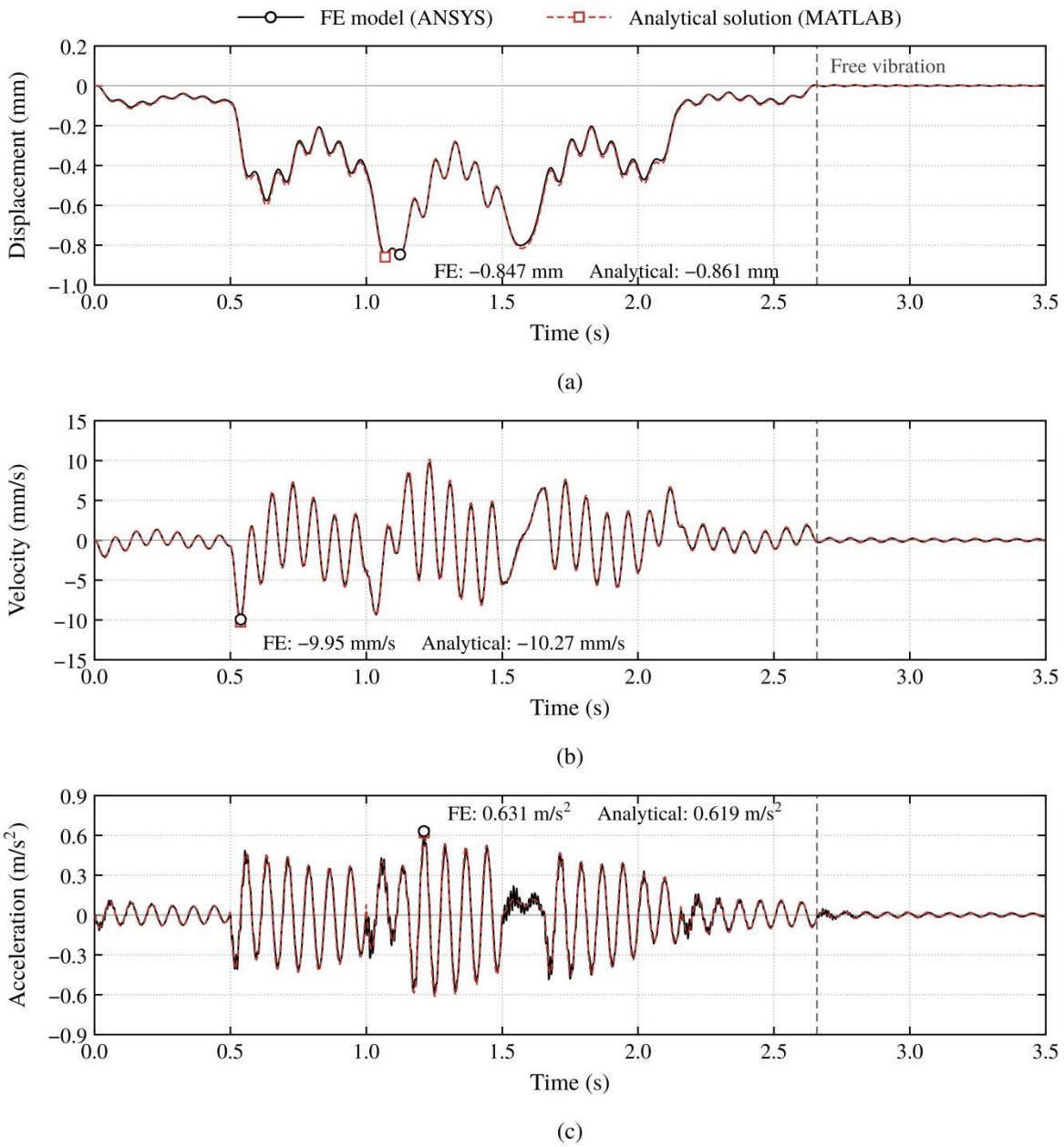


Fig. 9. Rigid-bond panel: FE (ANSYS) and closed-form (MATLAB) responses at the mid-span footprint S3 during the crossing and the subsequent free vibration: (a) displacement; (b) velocity; (c) acceleration. Downward is negative.

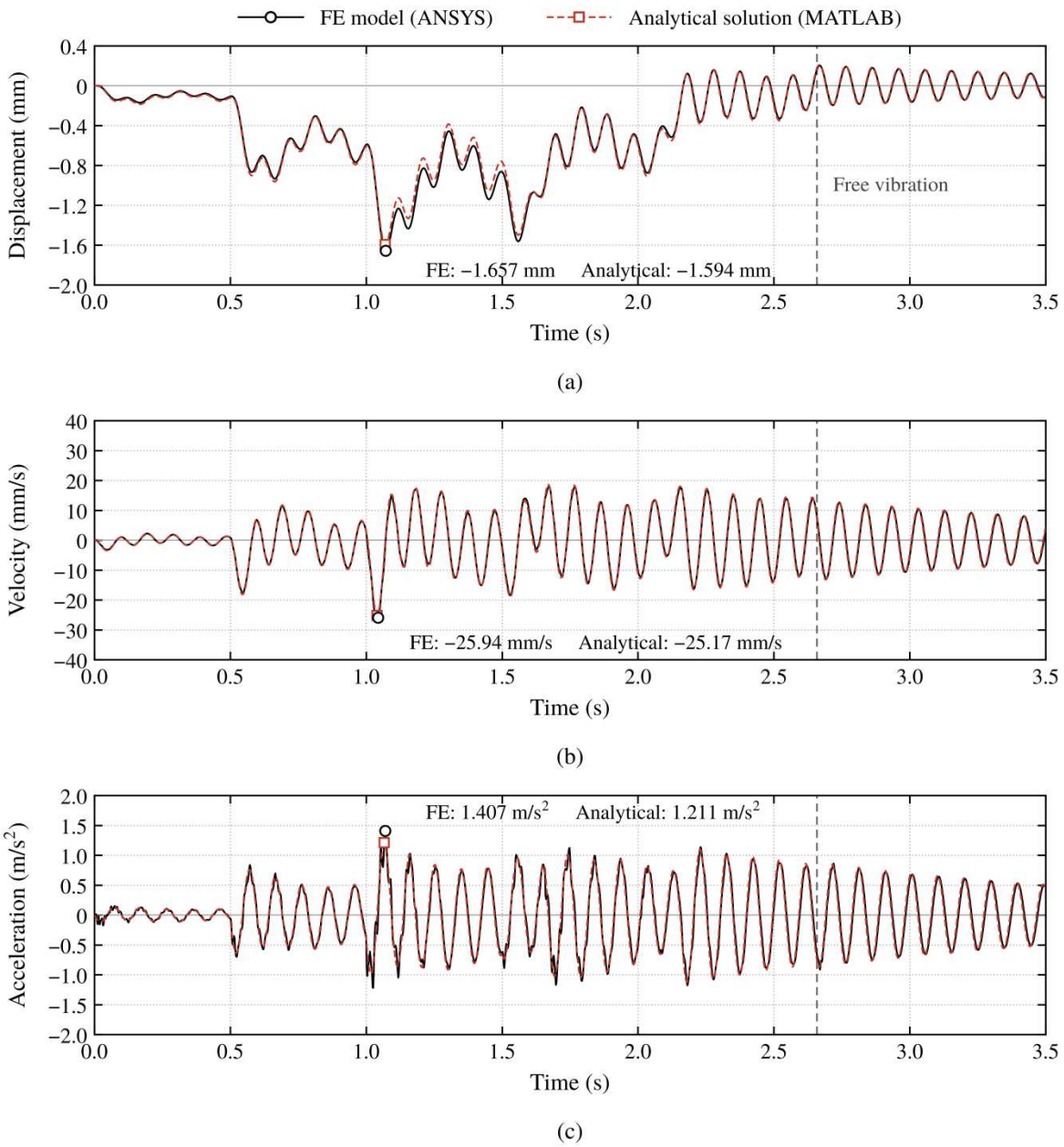


Fig. 10. Degraded-PVB panel: FE (ANSYS) and closed-form (MATLAB) responses at the mid-span footprint S3 during the crossing and the subsequent free vibration: (a) displacement; (b) velocity; (c) acceleration. Downward is negative.

Table 8. Comparison of the FE transient response with the closed-form solution at S3.

Panel	Quantity	FE peak (time)	Closed-form peak (time)	δ (%)	R^2	MAE
RB	u_z (mm)	−0.847 (1.124 s)	−0.861 (1.070 s)	−1.6	0.999	0.007 mm
RB	v_z (mm/s)	−9.95 (0.538 s)	−10.27 (0.538 s)	−3.1	0.997	0.13 mm/s
RB	a_z (m/s²)	0.631 (1.212 s)	0.619 (1.214 s)	+2.0	0.976	0.021 m/s²
DG	u_z (mm)	−1.657 (1.072 s)	−1.594 (1.070 s)	+3.9	0.992	0.026 mm
DG	v_z (mm/s)	−25.94 (1.044 s)	−25.17 (1.040 s)	+3.1	0.992	0.61 mm/s
DG	a_z (m/s²)	1.407 (1.070 s)	1.211 (1.066 s)	+16.1	0.968	0.074 m/s²

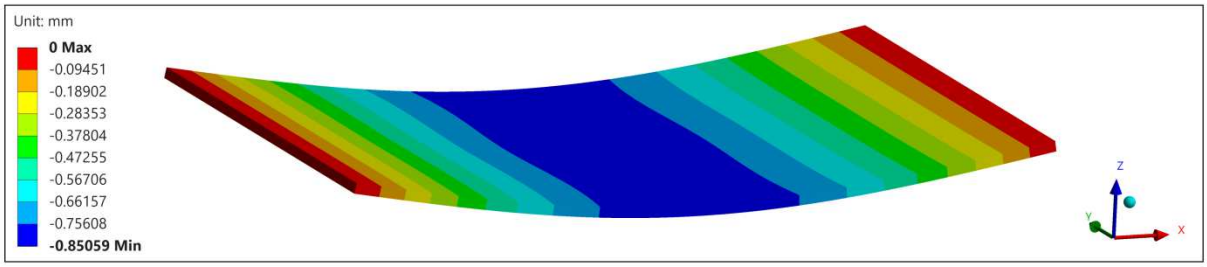
4.4 Transient response: effect of interlayer degradation

Table 9 compares the FE peak responses of the two panels. Degradation increases the peak displacement at S3 by a factor of 1.96 (−0.847 mm to −1.657 mm), the peak velocity by 2.61 (−9.95 mm/s to −25.94 mm/s), the peak acceleration by 2.23 (0.631 m/s² to 1.407 m/s²) and the peak principal stress in the glass by 1.61 (2.30 MPa to 3.70 MPa). The static displacement at S3 under the pedestrian's weight increases by a factor of only 1.70. The dynamic part of the response therefore grows more than the loss of stiffness alone would suggest, and the ratio of peak to static displacement rises from 1.47 to 1.69. The time histories in Figs. 9 and 10 show how the behaviour changes. The RB response follows the footfall sequence quasi-statically, with small superimposed oscillations that decay quickly, and the panel is practically at rest as soon as the pedestrian leaves (maximum upward displacement in free vibration 0.003 mm). The DG response builds up from step to step, and the panel keeps vibrating at its fundamental frequency after the crossing (0.203 mm). Fig. 11 shows the displacement and stress contours at the instants of peak response. The largest deflections of the whole panel, −0.851 mm for RB and −1.673 mm for DG, occur at mid-span and are close to the footprint values.

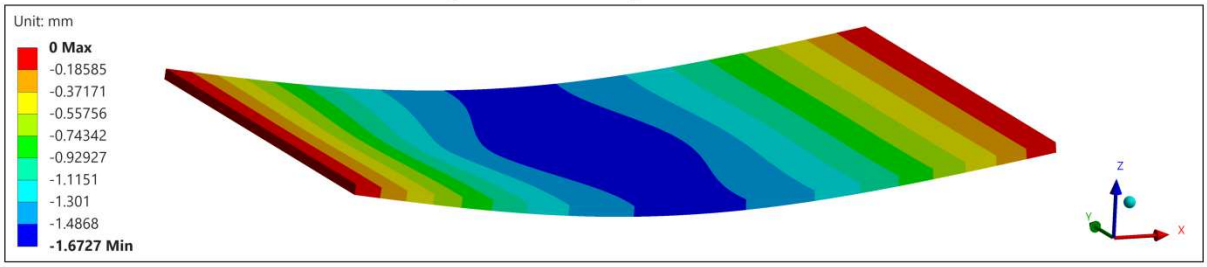
Table 9. Peak FE transient responses of the two panels to a pedestrian crossing.

Response	**RB**	**DG**	**DG/RB**
Peak displacement at S3, u_z (mm)	−0.847 (1.124 s)	−1.657 (1.072 s)	1.96
Largest displacement of the panel (mm)	−0.851	−1.673	1.97
Static displacement at S3 under $m_p g$ (mm)[a]	−0.58	−0.98	1.70
Peak velocity at S3, v_z (mm/s)	−9.95 (0.538 s)	−25.94 (1.044 s)	2.61
Peak acceleration at S3, a_z (m/s²)	0.631 (1.212 s)	1.407 (1.070 s)	2.23
Maximum principal stress in the glass (MPa)	2.30 (1.128 s)	3.70 (1.156 s)	1.61
Peak total support reaction (N)	1334 (0.564 s)	1540 (1.068 s)	1.15
Maximum upward displacement in free vibration (mm)	0.003	0.203	–

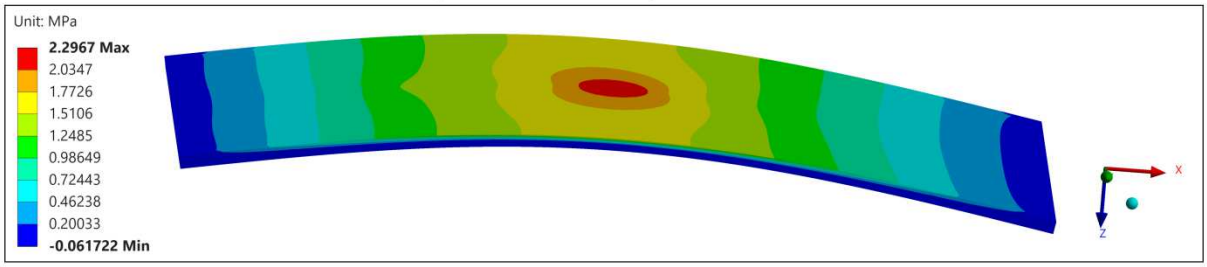
[a] From the quasi-static (1 Hz) value of the harmonic response, scaled to $m_p g$ = 784.8 N.



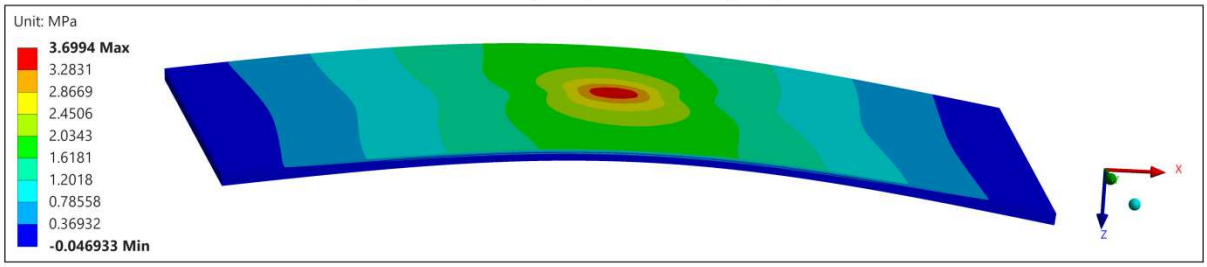
(a) Rigid bond: vertical displacement at 1.124 s



(b) Degraded PVB: vertical displacement at 1.072 s



(c) Rigid bond: maximum principal stress in the glass plies at 1.128 s



(d) Degraded PVB: maximum principal stress in the glass plies at 1.156 s

Fig. 11. Transient response at the instants of peak response: vertical displacement (a, b) and maximum principal stress in the glass plies viewed from below (c, d) of the rigid-bond and degraded-PVB panels. Deformed shapes are exaggerated for visibility.

5. Discussion

5.1 Interlayer degradation and natural frequencies

Both the FE and the analytical results show that the interlayer controls the dynamic behaviour of the panel. The PVB determines how far the glass plies act together: when it softens, less shear is transferred, the effective bending rigidity drops and every natural frequency falls with it. The reduction depends on the mode (Table 5). The fundamental frequency falls by 21%, whereas the higher bending and torsional modes fall by 42–53%, because the shear-coupling parameter g_i of Eq. (22) decreases with the square of the mode number. This mode

dependence is one reason why effective-thickness approaches, which replace the laminate by a single equivalent thickness, need frequency- or mode-dependent formulations in dynamics (López-Aenlle and Pelayo, 2014; Pelayo and López-Aenlle, 2019). The partial-interaction estimate of Eqs. (21)–(22) captures it with errors below 1% (Table 6) and does not require the section to be homogenised first.

Frequency shifts have already been used to diagnose the post-breakage loss of stiffness of in-service laminated glass units (Bedon and Noè, 2021). The present results show that a comparable shift can occur before any fracture, from interlayer softening alone. Since Eqs. (19)–(23) need only the geometry and the elastic moduli, they give a simple screening bracket for this panel: 12.97 Hz for full composite action and 4.06 Hz for independent plies. A measured fundamental frequency close to the upper bound points to an effective interlayer, whereas a frequency drifting towards the lower bound points to a loss of shear transfer consistent with PVB softening, ageing or moisture ingress. Eq. (23) then converts the measured frequency into an apparent interlayer shear modulus. In practice, support flexibility and non-structural layers also affect the measured frequency, so the bracket should be referred to a baseline measurement on the same structure. The measured frequency of the central-nave panels, 14.97 Hz (Bedon and Bergamo, 2019), for instance, is higher than both the RB model and the composite bound, which reflects support and system effects left out of the reduced panel model. For this reason, the study concentrates on the relative change between the two interlayer scenarios rather than on absolute frequencies.

5.2 Kinematic amplification under walking

Under walking, degradation amplifies velocity and acceleration (×2.61 and ×2.23) more than displacement (×1.96), although the resonant acceleration under the harmonic force did not change at all. The reason lies in how the two panels respond to the footfall sequence. Design guides separate low-frequency floors, whose fundamental frequency is below about four times the maximum step frequency (approximately 10 Hz) and which a walking harmonic can excite resonantly, from high-frequency floors, whose response to each footfall is a decaying impulse response (Smith et al., 2009; Willford and Young, 2006). With f_1 = 13.07 Hz, the RB panel belongs to the high-frequency group. The vibration triggered by each footfall decays between steps, and the response is dominated by the quasi-static deflection under the moving load. Degradation moves the fundamental frequency to 10.31 Hz, at the boundary between the two groups and close to the fifth harmonic of the 2.0 Hz step frequency. The DG panel

completes 5.16 natural cycles per step period, so the vibrations triggered by successive footfalls add up almost in phase. The RB panel completes 6.53 cycles per step, and successive footfalls partly cancel each other's vibration. This near-resonant build-up, visible in Fig. 10 and in the residual vibration after the crossing, raises the velocity and acceleration, which are dominated by the vibratory part of the response, more than the displacement, which is dominated by the quasi-static part. The higher modes of the DG panel, at much lower frequencies than those of the RB panel, add further to its peak acceleration (Section 4.3).

The amplification ratios therefore depend on the step frequency. At about 2.2 Hz, for example, the sixth harmonic would come close to the RB fundamental frequency and the ratios between the two panels would change. The general trend still holds: degradation lowers the fundamental frequency towards the stronger, lower-order walking harmonics and can turn a high-frequency panel into one that is excited resonantly. Displacement and stress checks, which are dominated by the quasi-static response, do not reveal this change on their own.

5.3 Glass stress

The maximum principal stress in the glass increases with degradation, by 14% at resonance and by 61% under walking. A laminated section that loses composite action is expected to behave this way. As less shear is transferred through the interlayer, each ply bends more and more about its own neutral axis; for the same bending moment, the extreme-fibre stress of three independent plies is 3.3 times that of the monolithic section, and the partially composite DG panel lies between these limits. Under walking, the stress grows less than the displacement (×1.61 against ×1.96) because the stress produced per unit curvature decreases as composite action is lost. The peak stress of the DG panel, 3.70 MPa, is about 3% of the characteristic bending strength of fully tempered glass, 120 MPa (CEN, 2015), and even the harmonic reference case (18.6 MPa) stays far below it. Glass strength therefore does not govern either panel under pedestrian loading.

5.4 Serviceability assessment

Table 10 summarises the serviceability checks based on the transient response to walking. The peak deflection of both panels is well within the adopted L/500 limit of 5.30 mm (16% and 32% utilisation), and the glass stress is small compared with the glass strength. It is the peak acceleration that separates the two panels. The RB panel (0.63 m/s²) meets the 0.7 m/s² limit recommended for the vertical vibration of footbridges in EN 1990 Annex A2 (CEN, 2002) and falls in the mean-comfort class of the Sétra guide (Sétra, 2006). The DG panel

(1.41 m/s²) exceeds this limit by a factor of two and falls in the minimum-comfort class. EN 1990 requires the comfort check only for vertical frequencies below 5 Hz, and frequency weighting of human perception would reduce the effective magnitudes at 10–13 Hz (ISO, 2007), so the limits are used here as indicative references. Even so, the comparison shows that, for this panel, vibration serviceability rather than deflection or glass strength becomes the governing criterion once the interlayer degrades. The harmonic amplitudes of Section 4.2 are not used in these checks, because a force held at resonance indefinitely does not represent a walking event on a panel whose fundamental frequency is five to six times the step frequency.

Table 10. Serviceability checks based on the transient response to a pedestrian crossing.

Criterion	Limit	RB	DG
Peak deflection	L/500 = 5.30 mm	0.85 mm (16%)	1.67 mm (32%)
Peak vertical acceleration	0.7 m/s² (CEN, 2002)	0.63 m/s²: satisfied	1.41 m/s²: exceeded
Comfort class (Sétra, 2006)	Maximum < 0.5; mean 0.5–1.0; minimum 1.0–2.5 m/s²	Mean	Minimum
Maximum principal stress in the glass	120 MPa (CEN, 2015)	2.30 MPa (1.9%)	3.70 MPa (3.1%)

5.5 Limitations

The model includes only the five-layer bonded laminate and leaves out the un-bonded top layer, steel tendons, gaskets and support flexibility of the real footbridge. The PVB is linear elastic within each scenario, whereas real PVB is viscoelastic, with properties that depend on temperature, load duration and frequency; the two scenarios represent a fully effective and a degraded state rather than reproducing this behaviour. The load is a single deterministic pedestrian at one step frequency, without gait variability, crowd effects or human–structure interaction, and the closed-form solution keeps only the fundamental mode. Future work should consider calibrated intermediate and frequency-dependent interlayer properties, explicit modelling of the supports and tendons, a range of step frequencies and pedestrian masses, and a frequency-weighted comfort assessment.

6. Conclusions

This study combined a closed-form multilayer plate solution with three-dimensional FE modal, harmonic and transient analyses to quantify how PVB interlayer degradation affects a five-layer laminated glass walkway panel under pedestrian excitation. The main conclusions are as follows.

1. The multilayer thin-plate formulation, solved in closed form by modal superposition and the Laplace transform, reproduces the FE transient response to a pedestrian crossing. The peak displacements agree within 1.6% (RB) and 3.9% (DG), and $R^2 \geq 0.99$ for displacement and velocity. Because the single-mode solution omits the higher modes, the FE peak acceleration of the degraded panel is 16% higher than the closed-form value.
2. Interlayer degradation (E_{PVB} reduced from 70 GPa to 4 MPa) lowers the fundamental frequency from 13.07 Hz to 10.31 Hz (−21%) and the higher-mode frequencies by 42–53%. The partial-interaction estimate reproduces the FE frequencies of the bending modes within 1%, and its inversion recovers the interlayer shear modulus within about 1%, which makes it a simple non-destructive screening tool.
3. Under a harmonic force at resonance, degradation increases the displacement amplitude by 61% and the velocity amplitude by 27%, while the acceleration amplitude stays the same because the modal mass does not change.
4. Under a pedestrian crossing at 2.0 Hz, degradation increases the peak displacement by a factor of 1.96, the peak velocity by 2.61, the peak acceleration by 2.23 and the peak glass stress by 1.61. Velocity and acceleration grow more than displacement because the lowered fundamental frequency approaches the fifth walking harmonic, so the vibrations triggered by successive footfalls add up.
5. The deflection of both panels stays well within L/500 and the glass stress below 4% of the strength of fully tempered glass, but the peak acceleration of the degraded panel, 1.41 m/s², is twice the 0.7 m/s² comfort limit. Vibration serviceability therefore governs the degraded panel, and assessments of existing laminated glass walkways should check the interlayer condition, the support restraint and the acceleration response together, not the glass stress alone.

Declaration of competing interest

The authors declare that they have no known competing financial interests or personal relationships that could have appeared to influence the work reported in this paper.

Data availability

Data will be made available on request.

References

ANSYS Inc., 2024. Ansys Mechanical APDL Theory Reference, Release 2024 R1. ANSYS Inc., Canonsburg, PA.

ASTM International, 2016. ASTM E1300-16, Standard Practice for Determining Load Resistance of Glass in Buildings. ASTM International, West Conshohocken, PA.

ASTM International, 2021. ASTM E2751/E2751M-21, Standard Practice for Design and Performance of Supported Laminated Glass Walkways. ASTM International, West Conshohocken, PA.

Bachmann, H., Ammann, W., 1987. Vibrations in Structures: Induced by Man and Machines. Structural Engineering Documents 3e. International Association for Bridge and Structural Engineering (IABSE), Zürich.

Bathe, K.J., 1996. Finite Element Procedures. Prentice Hall, Englewood Cliffs, NJ.

Bedon, C., 2019. Diagnostic analysis and dynamic identification of a glass suspension footbridge via on-site vibration experiments and FE numerical modelling. Compos. Struct. 216, 366–378.

Bedon, C., Bergamo, E., 2019. Vibration experiments for diagnostic investigations on a glass suspension footbridge. Vibroeng. Procedia 24, 41–46.

Bedon, C., Fasan, M., 2019. Reliability of field experiments, analytical methods and pedestrian's perception scales for the vibration serviceability assessment of an in-service glass walkway. Appl. Sci. 9(9), 1936.

Bedon, C., Fasan, M., Amadio, C., 2019. Vibration analysis and dynamic characterization of structural glass elements with different restraints based on operational modal analysis. Buildings 9(1), 13.

Bedon, C., Mattei, S., 2021. Facial expression-based experimental analysis of human reactions and psychological comfort on glass structures in buildings. Buildings 11(5), 204.

Bedon, C., Noè, S., 2021. Post-breakage vibration frequency analysis of in-service pedestrian laminated glass modular units. Vibration 4(4), 836–852.

Caprani, C.C., Keogh, J., Archbold, P., Fanning, P., 2012. Enhancement factors for the vertical response of footbridges subjected to stochastic crowd loading. Comput. Struct. 102–103, 87–96.

CEN, 2002. EN 1990:2002+A1:2005, Eurocode – Basis of structural design (Annex A2: Application for bridges). European Committee for Standardization, Brussels.

CEN, 2005. EN 14449:2005, Glass in building – Laminated glass and laminated safety glass – Evaluation of conformity/Product standard. European Committee for Standardization, Brussels.

CEN, 2015. EN 12150-1:2015, Glass in building – Thermally toughened soda lime silicate safety glass – Part 1: Definition and description. European Committee for Standardization, Brussels.

CEN, 2021. CEN/TS 19100-1:2021, Design of glass structures – Part 1: Basis of design and materials. European Committee for Standardization, Brussels.

Chopra, A.K., 2017. Dynamics of Structures: Theory and Applications to Earthquake Engineering, fifth ed. Pearson, Hoboken, NJ.

Clough, R.W., Penzien, J., 1993. Dynamics of Structures, second ed. McGraw-Hill, New York.

CNR, 2013. CNR-DT 210/2013, Istruzioni per la progettazione, l'esecuzione ed il controllo di costruzioni con elementi strutturali di vetro. National Research Council of Italy, Rome (in Italian).

Cook, R.D., Malkus, D.S., Plesha, M.E., Witt, R.J., 2002. Concepts and Applications of Finite Element Analysis, fourth ed. Wiley, New York.

Fan, J.S., Chen, Y., Nie, J.G., 2012. Modeling and validation of pedestrian-induced walking load on footbridges. Chin. J. Comput. Mech. 29(4), 538–544 (in Chinese).

Feldmann, M., Kasper, R., Abeln, B., et al., 2014. Guidance for European Structural Design of Glass Components. JRC Scientific and Policy Report EUR 26439 EN. Publications Office of the European Union, Luxembourg.

Galuppi, L., Royer-Carfagni, G., 2012. Effective thickness of laminated glass beams: New expression via a variational approach. Eng. Struct. 38, 53–67.

Gong, M., Li, Y., Shen, R., Wei, X., 2021. Glass suspension footbridge: Human-induced vibration, serviceability evaluation, and vibration mitigation. J. Bridge Eng. 26(11), 05021014.

ISO, 2007. ISO 10137:2007, Bases for design of structures – Serviceability of buildings and walkways against vibrations. International Organization for Standardization, Geneva.

Kim, S.M., 2004. Influence of horizontal resistance at plate bottom on vibration of plates on elastic foundation under moving loads. Eng. Struct. 26(4), 519–529.

López-Aenlle, M., Pelayo, F., 2014. Dynamic effective thickness in laminated-glass beams and plates. Compos. Part B Eng. 67, 332–347.

Newmark, N.M., 1959. A method of computation for structural dynamics. J. Eng. Mech. Div. 85(3), 67–94.

Newmark, N.M., Siess, C.P., Viest, I.M., 1951. Tests and analysis of composite beams with incomplete interaction. Proc. Soc. Exp. Stress Anal. 9(1), 75–92.

Pachi, A., Ji, T., 2005. Frequency and velocity of people walking. Struct. Eng. 83(3), 36–40.

Pelayo, F., López-Aenlle, M., 2019. Natural frequencies and damping ratios of multi-layered laminated glass beams using a dynamic effective thickness. J. Sandw. Struct. Mater. 21(2), 439–463.

Qin, J.W., Law, S.S., Yang, Q.S., Yang, N., 2013. Pedestrian–bridge dynamic interaction, including human participation. J. Sound Vib. 332(4), 1107–1124.

Racic, V., Pavic, A., Brownjohn, J.M.W., 2009. Experimental identification and analytical modelling of human walking forces: Literature review. J. Sound Vib. 326(1–2), 1–49.

Ramoul, A., Spremić, M., 2021. Vibration serviceability limit state of pedestrian bridges. Građevinski materijali i konstrukcije 64(3), 177–183.

Sétra, 2006. Footbridges: Assessment of Vibrational Behaviour of Footbridges under Pedestrian Loading. Technical guide. Service d'Études Techniques des Routes et Autoroutes, Paris.

Shahabpoor, E., Pavic, A., Racic, V., 2016. Interaction between walking humans and structures in vertical direction: A literature review. Shock Vib. 2016, 3430285.

Smith, A.L., Hicks, S.J., Devine, P.J., 2009. Design of Floors for Vibration: A New Approach, revised ed. SCI Publication P354. The Steel Construction Institute, Ascot.

Van Nimmen, K., Lombaert, G., De Roeck, G., Van den Broeck, P., 2014. Vibration serviceability of footbridges: Evaluation of the current codes of practice. Eng. Struct. 59, 448–461.

Willford, M.R., Young, P., 2006. A Design Guide for Footfall Induced Vibration of Structures. CCIP-016. The Concrete Centre, Camberley.

Yan, Z.D., 1989. Fourier Series Solutions in Structural Mechanics. Tianjin University Press, Tianjin (in Chinese).

Zhang, Z.D., Ma, D.W., He, Q., Zhu, Z.L., 2015. Dynamic response of multi-layer rectangle plate on two-parameter foundation model under circular rigid bearing plate load. J. Vib. Shock 34(17), 199–206 (in Chinese).

Živanović, S., Pavic, A., Reynolds, P., 2005. Vibration serviceability of footbridges under human-induced excitation: a literature review. J. Sound Vib. 279(1–2), 1–74.